

Heteroalkyl-Substitution in Molecular Organic Semiconductors: Chalcogen Effect on Crystallography, Conformational Lock, and Charge Transport

Shakil N. Afraj, Chia-Chi Lin, Arulmozhi Velusamy, Chang-Hui Cho, Hsin-Yi Liu, Jianhua Chen, Gene-Hsiang Lee, Jui-Chen Fu, Jen-Shyang Ni, Shih-Huang Tung, Shuehlin Yau, Cheng-Liang Liu,* Ming-Chou Chen,* and Antonio Facchetti*

The effect of heteroalkyl (-XR, X = Se, S, O) substitution on a series of molecular semiconductors having a 3,3'-diheteroalkyl-2,2'-bithiophene (XBT) central core is studied. Thus, the selenotetradecyl (-SeC₁₄H₂₉) SeBT core is investigated by end-functionalization with two dithienothiophene (DTT), thienothiophene (TT), and thiophene (T) units to give SeBTs 1–3, respectively, for molecular π -conjugation effect examination. Furthermore, the selenodecyl (-SeC₁₀H₂₁) and selenohexyl (-SeC₆H₁₃) SeBT cores end-capped with DTTs to give SeBTs 1B and 1C, respectively, are synthesized for understanding -SeR length effects. To address systematically the impact of the chalcogen heteroatom, the newly developed selenoalkyl SeBTs are compared with the previously reported thiotetradecyl (-SC₁₄H₂₉) DDTT-SBT (4) and the new tetradecyloxy (-OC₁₄H₂₉) DDTT-OBT (5). When fabricating organic field effect transistors by the solution-shearing method, the devices based on the tetradecylated DDTT-SeBT (1) exhibit the highest mobility up to 4.01 cm² V⁻¹ s⁻¹, which is larger than those of the other SeBT compounds and both DDTT-SBT (4) (1.70 cm² V⁻¹ s⁻¹) and DDTT-OBT (5) (9.32 × 10⁻⁴ cm² V⁻¹ s⁻¹). These results are rationalized by a combination of crystallographic, morphological, and microstructural analysis.


1. Introduction

Organic semiconductors comprising π -conjugated units have been the subject of considerable scientific and industrial research because of their potential applications in various optoelectronic and energy devices such as flexible displays, sensors, solar cells, and batteries as well as in biomedical applications.^[1–28] Particularly, several studies have addressed the development of organic small molecules for organic field effect transistors (OFETs), enabling electronic circuit fabrication via inexpensive and potentially high-throughput solution processes compared with vacuum deposition typical of silicon devices.^[29–37] Organic small molecules are interesting because of well-defined molecular structure, simple purification, and good batch to batch reproducibility as compared to many organic polymers.^[38–41] To design novel solution processable small

S. N. Afraj, A. Velusamy, C.-H. Cho, H.-Y. Liu, J.-C. Fu, S. Yau, M.-C. Chen
Department of Chemistry
and Research Center of New Generation Light Driven
Photovoltaic Modules
National Central University
Taoyuan 32001, Taiwan
E-mail: mcchen@ncu.edu.tw

C.-C. Lin
Department of Chemical and Materials Engineering
National Central University
Taoyuan 32001, Taiwan

C.-C. Lin
Department of Applied Chemistry
Graduate School of Advance Science and Engineering
Hiroshima University
Higashi-Hiroshima, Hiroshima 739-8527, Japan

 The ORCID identification number(s) for the author(s) of this article can be found under <https://doi.org/10.1002/adfm.202200880>.

© 2022 The Authors. Advanced Functional Materials published by Wiley-VCH GmbH. This is an open access article under the terms of the Creative Commons Attribution License, which permits use, distribution and reproduction in any medium, provided the original work is properly cited.

DOI: 10.1002/adfm.202200880

J. Chen, A. Facchetti
Department of Chemistry
Northwestern University
Evanston, IL 60208, USA
E-mail: a-facchetti@northwestern.edu

G.-H. Lee
Instrumentation Center
National Taiwan University
Taipei 10617, Taiwan

J.-S. Ni
Department of Chemical and Materials Engineering
Photo-sensitive Material Advanced Research and Technology Center
(Photo-SMART)
National Kaohsiung University of Science and Technology
Kaohsiung 80778, Taiwan

S.-H. Tung
Institute of Polymer Science and Engineering
National Taiwan University
Taipei 10617, Taiwan

C.-L. Liu
Department of Materials Science and Engineering
National Taiwan University
Taipei 10617, Taiwan
E-mail: liucl@ntu.edu.tw

molecules several factors need to be considered to enhance charge transport, particularly, they must contain a planar conjugated core to promote π - π stacking through intermolecular orbital overlap, proper orbital energetic for stable charge transport, and have substituents for solution processability.^[34,37,42,43] Based on these requirements, considerable progress has been made in advancing π -conjugated small molecules.^[44–46] Among them, fused-thiophene-based small molecules have been widely explored due to the highly planar structures, strong intermolecular S \cdots S interactions and extensive π -conjugation.^[47–51]

Alkyl chain functionalization of semiconductor cores and modification of the chain pattern by changing the length, installing branching points, and altering the branching position has been instrumental to optimize device performance of solution processed semiconductors. Chemical modifications of alkyl substituents can strongly affect molecular core conformation, molecular properties, as well as packing and intermolecular interactions of the corresponding organic semiconductors.^[47,52–54] Heteroatoms have also been utilized to bridge a thiophene/molecular unit with an alkyl chain as well as introduced at different position of the alkyl substituent.^[47–50,55] The use of a heteroatom (X) and its location in the chain strongly affect energetic states, molecular conformation, solubility, and film wettability.^[47,55,56] For instance, when replacing a $-\text{CH}_2-$ group in 3,3'-dialkyl-2,2'-dithiophene with an $-\text{S}-$ linker in 3,3'-dithioalkyl-2,2'-dithiophene the latter structure is completely planar and, when integrated into larger molecular motifs, it retains substantial solubility in several organic solvents. This is the result of strong intramolecular S(alkyl) \cdots S(thio) interactions, also known as intramolecular lock, favoring solid state planarization of several small molecular and polymeric systems.^[47–49,55] This successful strategy has been expanded to other heteroatoms (e.g., X = O, F; **Figure 1a**) and evidence of planarization by crystal structure analysis reported in a few studies.^[56–63]

Furthermore, heteroatom-promoted molecular orbital delocalization has been shown to improve device performances.^[55] However, to the best of our knowledge, extension to selenium (Se) in this intramolecular lock series has never been accomplished. Selenium-containing organic semiconductors have paved the way to new high-performance OFETs typically using selenophene as the key building block.^[64–68] Particularly, several studies have demonstrated p-type OFETs with excellent performance.^[69–77] For instance, Takimiya and co-workers reported [1]benzoselenopheno[3,2-*b*][1]benzoselenophene (**BSBS**) small molecule-based single crystals OFET with hole mobility of $0.70 \text{ cm}^2 \text{ V}^{-1} \text{ s}^{-1}$.^[73] To the best of our knowledge, the same group also investigated the only known -SeMe substituted small-molecular semiconductors, 3,7-bis(methylthio)benzo[1,2-*b*:4,5-*b'*]dithiophene (**MT-DBT**) and 3,7-bis(methylseleno)benzo[1,2-*b*:4,5-*b'*]dithiophene (**BS-BDT**) for OFETs.^[78] Devices based on single crystals of these semiconductors exhibited field effect hole mobilities of 0.87 and $0.32 \text{ cm}^2 \text{ V}^{-1} \text{ s}^{-1}$, respectively. Furthermore, Okamoto et al. reported alkyl substituted selenium bridged V-shaped organic semiconductor exhibit impressive carrier mobility up to $11 \text{ cm}^2 \text{ V}^{-1} \text{ s}^{-1}$ (**Figure 1b**). Equally impressive, Heeney and co-workers reported selenophene-based polymeric OFETs, such as poly(3-dodecyl selenophene-vinylene) (**P3SV**),^[79] 2,5-di(2-octyl-dodecyl)-3,6-bis-(5-bromoselenyl)-1,4-diketopyrrolo[3,4-*c*]pyrrole-benzothiadiazole

(**PSeDPPBT**),^[80] indacenodiselenophene-2,1,3-benzothiadiazole (**PIDSeBT**)^[64] with hole mobilities of 0.05 , 0.46 , and $6.4 \text{ cm}^2 \text{ V}^{-1} \text{ s}^{-1}$, respectively. Shim and co-workers prepared poly(5,5'-bis(3-dodecylthiophen-2-yl)-2,2'-bisenophene) (**PDT2Se2**)^[81] and demonstrated FETs with a hole mobility of $0.02 \text{ cm}^2 \text{ V}^{-1} \text{ s}^{-1}$ (**Figure 1c**), while Jang and co-workers reported that the small molecule selenophene-vinylene-selenophene linker donor unit (**N-SVS-N**)^[82] exhibited an electron mobility up to $0.016 \text{ cm}^2 \text{ V}^{-1} \text{ s}^{-1}$. On the polymer front, Jenekhe and co-workers reported poly(naphthalene diimide-*alt*-bisenophene) (**PNDIBS**),^[83] which exhibits a high field effect electron mobility of $0.07 \text{ cm}^2 \text{ V}^{-1} \text{ s}^{-1}$ (**Figure 1d**). Despite these instrumental successes, selenophene is an expensive heterocycle, which costs ranges $\approx 10\times$ that of thiophene, and thus a cheaper Se incorporation strategy to new Se-containing materials would be preferred.

In this study we envisioned Se incorporation as a linker of alkyl substituent while retaining the bithiophene (BT)-based core with the hope to preserve Se(alkyl) \cdots S(thio) intramolecular lock (to ensure a planar BT central unit) in SeBT semiconductors as well as enable a more cost-effective synthesis of Se-containing molecules.

Our design also took into account our recent study involving the thioalkyl-substituted BT (SBT) unit end-capped with two dithienothiophene (DTT) units afforded molecules with OFET hole mobilities as high as $1.70 \text{ cm}^2 \text{ V}^{-1} \text{ s}^{-1}$ ^[47] and DSSCs (SBT-6) with power conversion efficiencies up to 9.47% .^[84,85] Thus, herein we report a strategy for incorporating Se by end-capping the SeBT unit with different heteroarenes including DTT, thienothiophene (TT), and thiophene (T) for studying -SeR and π -core variations in this series (compounds **1–3**, **Figure 2**). Furthermore, to address how heteroalkyl functionalization along the chalcogen (O, S, Se) series affects molecular structure and charge transport, we investigated and contrasted the properties of the selenoalkyl **DDTT-SeBT** (**1**) with the corresponding thioalkyl **DDTT-SBT** (**4**) and alkoxy **DDTT-OBT** (**5**) (**Figure 2**). Analysis of thermal, optical, electrochemical and charge transport properties of **1–3** underscore the effect of π -conjugation in selenoalkyl-substituted derivatives while contrasting the properties of **1**, **4**, and **5**, coupled with molecular orbital computations and crystal structure analysis, points to chalcogen effect as a substituent. Importantly, the crystal structures of **1**, **4**, and **5** demonstrate that intramolecular locks are equally effective in planarizing the XBT units even when using the large selenium atom, thus, independently of the chalcogen type. Thin-films of **1–5** were fabricated by solution-shearing and film morphology, microstructure, and charge transport investigated by atomic force microscope (AFM), grazing-incidence X-ray diffraction (GIXRD), and in OFETs. Among these series, devices based on the selenotetradecyl-substituted molecule **DDTT-SeBT** (**1**) exhibit the best performance with the highest hole mobility surpassing $4.0 \text{ cm}^2 \text{ V}^{-1} \text{ s}^{-1}$, which is the greatest value reported to date for all/fused-thiophene semiconductors.

2. Results and Discussion

In this section we first report the synthesis of the new SeBT- and OBT-based small molecules followed by evaluation of their physical properties using several characterization techniques. Next, we compare and contrast the molecular structure and packing

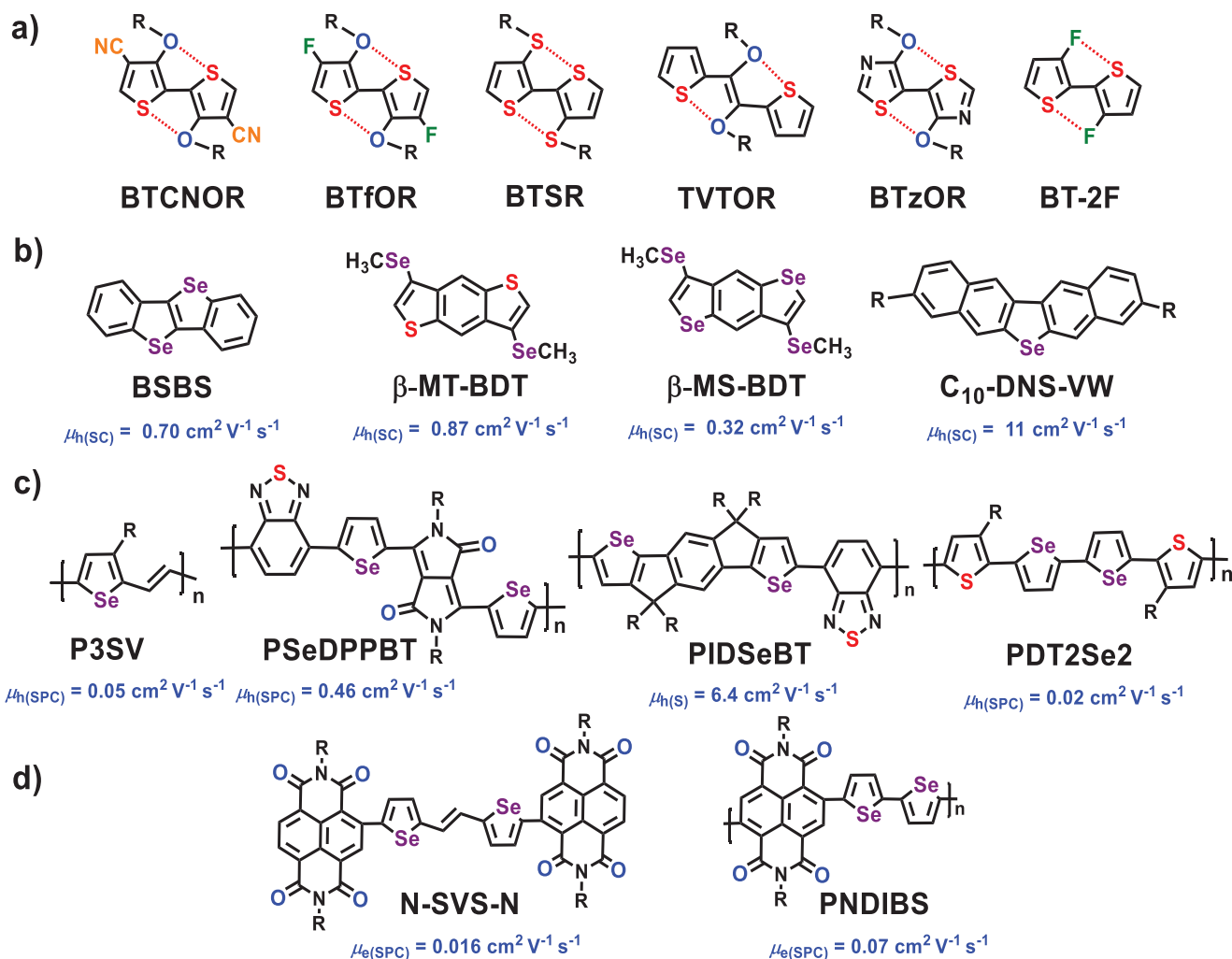


Figure 1. a) Building blocks containing S-X interactions (X = S, O, F). b-d) Selected selenium containing small molecular, and polymeric semiconductors for OFETs. μ_h and μ_e denote hole and electron mobilities in $\text{cm}^2 \text{ V}^{-1} \text{ s}^{-1}$, respectively. (S), (SC), and (SPC) denote semiconductor films obtained from solution-shearing deposition, single crystal process, and spin-coating deposition, respectively.

characteristics of heteroalkyl-functionalized XBT compounds using single crystal analysis. Then, thin films of all organic semiconductors were fabricated by using solution-shearing processing and their charge transport properties evaluated in FET devices. Finally, we characterize the organic semiconductor film morphology and microstructure to rationalize, in combination with the molecular computations, physical and single crystal data as well as trends in charge transport characteristics.

2.1. Synthesis

The synthetic route to all new SeBTs is reported in **Scheme 1** (see also Schemes S1 and S2 of the Supporting Information for synthetic details). The new selenoalkyl-functionalized SeBT cores were prepared from lithiation of 3-bromothiophene (**6**) and treatment with elemental selenium, followed by alkylation to afford selenoalkylated thiophenes **7A–7C**. The latter then undergo homocoupling reaction in the presence of $\text{ZnCl}_2/\text{CuCl}_2$ ^[86] to produce selenoalkyl bithiophenes **8A–8C**. The selenotetradecyl SeBT core (**8A**) was stannylated to afford

compound **9A**, then it was end-capped with mono-brominated DTT, TT, and T, via Stille cross coupling reactions, to give SeBTs **1–3**, respectively. Then shorter selenoalkyl SeBT cores (**8B** and **8C**) were stannylated to afford compound **9B** and **9C**. Reaction of the stannylated selenodecyl and selenohexyl SeBT cores with mono-brominated dithienothiophene (**10**)^[51,87,88] afforded SeBTs **1B** and **1C**, respectively, with central SeBT core bearing shorter alkyl chains. Therefore, the effect of π -conjugated end-capping units and side chains length can be systematically studied. To systematically compare the new selenoalkylated SeBT derivatives and the previously reported thioalkylated DDTT-SBT (**4**)^[47] the new alkoxyated DDTT-OBT (**5**) was prepared and the synthetic route is depicted in Scheme S3 of the Supporting Information. Synthetic details can be found in the Supporting Information.

2.2. Physical Characterization

The thermal properties of compounds **1–5** were evaluated using differential scanning calorimetry (DSC, Figure S1, Supporting Information) and thermogravimetric analysis (TGA,

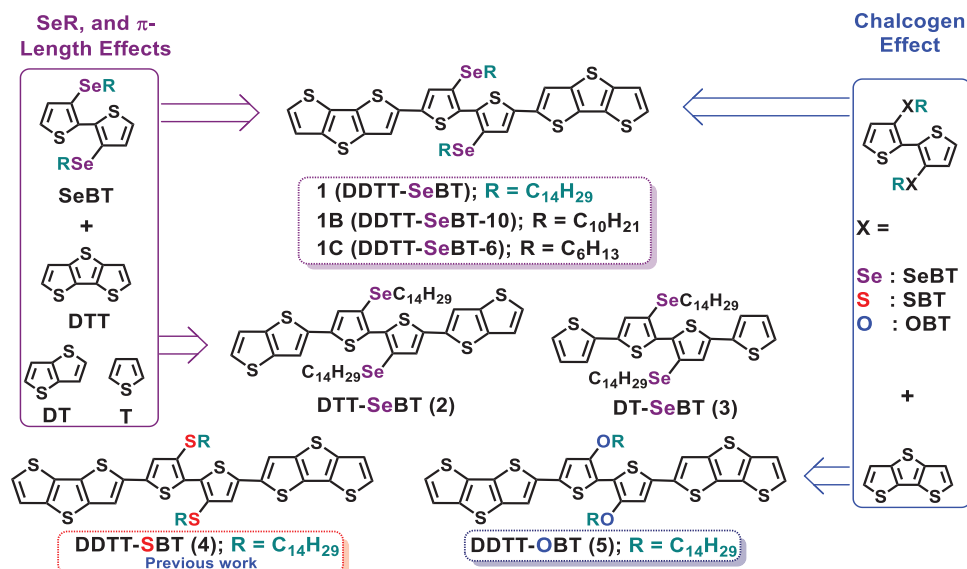
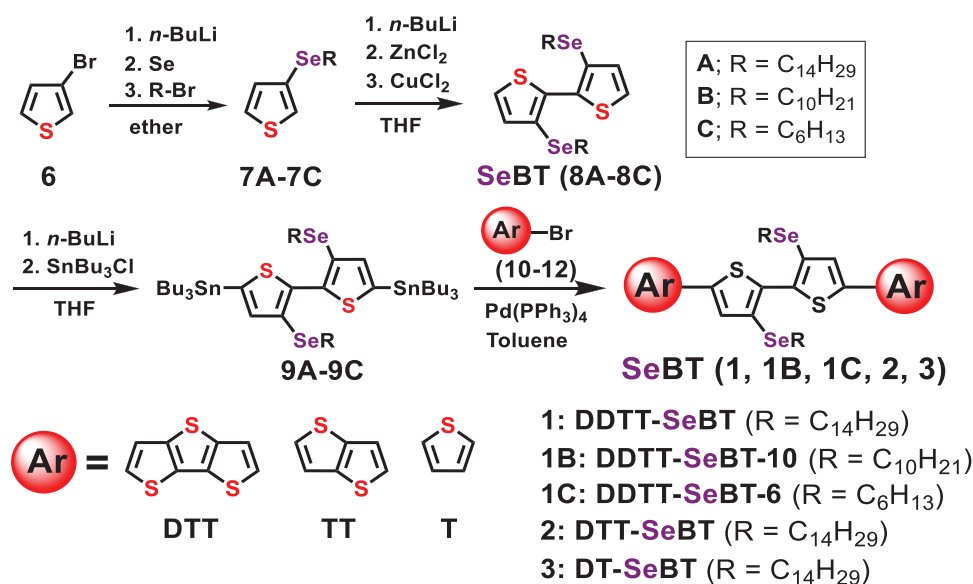


Figure 2. Strategies to XBT-based semiconductors (1–5) investigated in this study.

Figure S2, Supporting Information). As reported in Table 1, DSC data show that the melting temperature (T_m) of SeBT-based compounds varies when using different end-capping units and different selenoalkyl chain length. For the DDTT-SeBTs, when the side chain length decreases from $-C_{14}H_{29}$ (1) to $-C_{10}H_{21}$ (1B) and $-C_6H_{13}$ (1C), the T_m increases from 127 to 135 and 154 °C, respectively. By contrast, decreasing the end-capping conjugation length from DTT (1) to TT (2) to T (3), the T_m of 1 is strongly decreased by ≈ 60 °C, suggesting that intermolecular interactions are promoted when the largest end-capping groups are introduced. Furthermore, comparing the effect of the chalcogen in the DDTT-XBT series, the melting temperature slightly decreases in the order of 4 (140 °C) > 5 (137 °C) > 1 (127 °C). This trend is similar to that observed

going from fused thiophenes to fused selenophenes (e.g., BTBT (mp = 220 °C) to BSBS (mp = 210 °C))^[73] but, interestingly, differs to that seen going from oligothiophenes to oligofuranes to oligoselenophenes (e.g., 6T (mp = 310 °C), 6F (mp = 261 °C), 6Se (mp = 307 °C)).^[89–91] TGA analysis reveals that all three DDTT-SeBT compounds (1, 1B, and 1C) exhibit good thermal stability with $\approx 5\%$ weight loss occurring at a temperature (T_d) greater than 280 °C. When the side chain length decreases from $-C_{14}H_{29}$ to $-C_{10}H_{21}$, and $-C_6H_{13}$, the T_d of compounds 1, 1B, and 1C slightly increases from 282 to 298 and 299 °C, respectively. Interestingly to note that T_d correlates well with the conjugation dimension of the end-capping unit, with T_d increasing from DT-SeBT (3; ≈ 260 °C) to DTT-SeBT (2; ≈ 270 °C) to DDTT-SeBT (1–1C; ≈ 280 –300 °C). However, among the three



Scheme 1. Synthetic route to the SeBT-based final compounds.

Table 1. Thermal, optical, and electrochemical properties of the indicated compounds.

Cpd	$T_m^a)$ [°C]	$T_d^b)$ [°C]	$\lambda_{max}^c)$ sol [nm]	$\lambda_{max}^d)$ film [nm]	$E_g^e)$ sol [eV]	$E_g^f)$ film [eV]	$E_{ox}^g)$ [V]	$E_{red}^g)$ [V]	$E_{HOMO}^h)$ [eV]	$E_{LUMO}^i)$ [eV]	$E_g^j)$ [eV]
1	127	282	406	504	2.39	1.88	0.92	-1.69	-5.12	-2.50	2.62
1B	135	298	403	504	2.39	1.99	0.92	-1.69	-5.12	-2.50	2.62
1C	154	299	403	466	2.39	2.07	0.92	-1.69	-5.12	-2.50	2.62
2	57	270	385	396	2.51	2.35	0.98	-1.75	-5.18	-2.45	2.73
3	63	261	358	373	2.66	2.53	1.02	-1.88	-5.22	-2.32	2.89
4	140	352	438	504	2.35	1.91	0.87	-1.62	-5.07	-2.58	2.49
5	137	321	479	434	2.26	2.06	0.59	n.d. ^{k)}	-4.79	-2.53 ^{l)}	n.d. ^{k)}

^{a)}By DSC; ^{b)}By TGA; ^{c)}Absorption spectra were measured in *o*-C₆H₄Cl₂; ^{d)}Thin films were solution-sheared onto quartz glass; ^{e)}Optical energy bandgap was calculated by $1240/\lambda_{onset}$; ^{f)}Thin-film optical energy bandgap was calculated by $1240/\lambda_{onset}$; ^{g)}By DPV in *o*-C₆H₄Cl₂, E_{ox} = oxidative potential; E_{red} = reductive potential; ^{h)} $E_{HOMO} = -(4.2 + E_{ox})$; ⁱ⁾ $E_{LUMO} = -(4.2 + E_{red})$; ^{j)}Energy gap obtained by DPV; ^{k)}Not determined; ^{l)}Estimated from $E_{HOMO} + E_g$.

heteroalkyl-BT organic semiconductors, **DDTT-SBT** (4) and **DDTT-OBT** (5) exhibit a higher thermal stability, with a T_d at 352 and 321 °C, respectively.

The optical absorption properties of 1–5 were studied by UV–vis measurements. The normalized absorption spectra of diluted solutions and thin films were measured at room temperature and are plotted in **Figure 3a–d**, with the corresponding data summarized in Table 1. When going from solution to film state, there is a significant bathochromic shift of the absorption onset (λ_{on}) and, except for compound 5 (vide infra), the absorption maximum (λ_{max}) of all the compounds. Furthermore, for those having larger cores, formation of a multiband profile absorption is evident, suggesting core planarization, promoted by intramolecular lock, and molecular aggregation in the solid state. Specifically, as seen in **Figure 3a**, the solution state absorption spectra of compounds 1, 1B, and 1C are featureless and almost identical ($\lambda_{max} = 403–406$ nm) suggesting that side chain length variations do not have strong influences on the **DDTT-SeBT** molecular core absorption. However, in the solid-state, the absorption of 1C broadens considerably but remains featureless versus those of 1 and 1B (**Figure 3b**), which feature well-defined 0–0 transitions, likely because the shorter

chain has less tendency to form order lamellar structures, thus reducing overall order.^[92] The absorption peaks of both solution and solid states gradually red-shift moving from 3 to 2 to 1, in agreement with the enhanced π -conjugation of the molecular core by incorporation of more π -extended end-capping units to the central SeBT units. The calculated optical bandgap (E_g , determined from onset of absorption) of **DDTT-SeBT** compounds 1, 1B, and 1C in solution and in the solid state are almost identical and found to be ≈ 2.4 and ≈ 2.0 eV, respectively. Unsurprisingly, when looking at the E_g in solution/film going from 3 (2.66/2.53 eV) to 2 (2.51/2.35 eV) and particularly to 1 (2.39/1.88 eV), it is clear that π -extension promotes intramolecular electron delocalization. When analyzing the chalcogen effect, the solution absorption peak maximum of **DDTT-OBT** (5) (479 nm) is considerably red-shifted as compared to those of **DDTT-SBT** (4) (438 nm) and **DDTT-SeBT** (1) (406 nm) (**Figure 3c**), due to the strong electron donating effect on central bithiophene of the alkoxy versus thio/selenaalkyl side chains as well as lower steric demand of the small oxygen versus larger S and Se atoms, resulting in a statistically more planar core conformation in solution (vide infra).^[58] However, when moving from the solution to the solid state, the optical profile

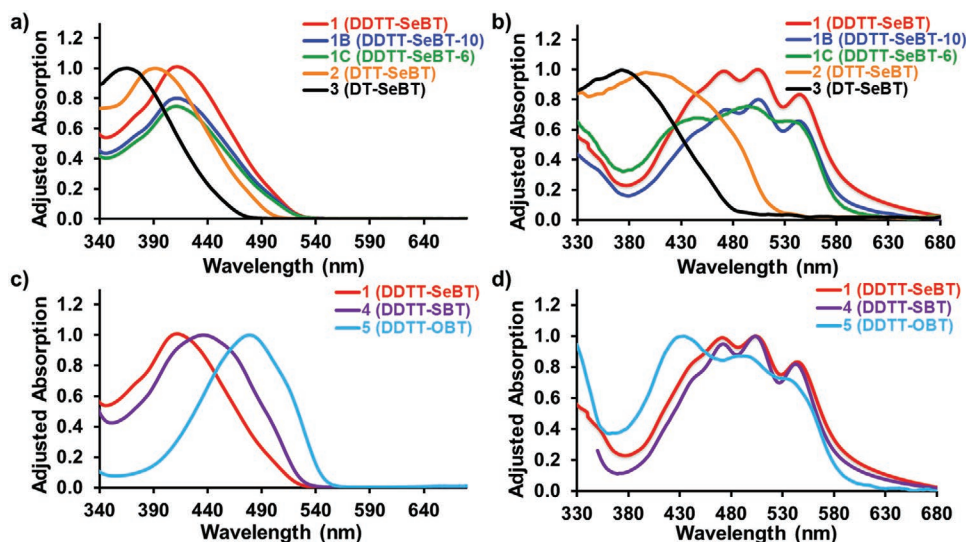


Figure 3. Normalized UV–vis absorption spectra of 1–5 (with the exception of 1B and 1C to enhance clarity) in a,c) diluted solution and b,d) thin film.

and transition band maxima of the **DDTT-OBT** (**5**) are considerably different than those of **DDTT-SBT** (**4**) and **DDTT-SeBT** (**1**) derivatives, with the former evidencing a blue-shifted λ_{max} by ≈ 50 nm versus a red-shifted absorption by ≈ 60 and ≈ 90 nm for the latter two compounds, respectively (Figure 3d).

The solid-state absorption profile also differs and is consistent with formation of *H*-aggregates for **DDTT-OBT** (**5**) versus *J*-aggregates for both **DDTT-SBT** (**4**) and **DDTT-SeBT** (**1**),^[93] a phenomena supported by the molecular packing accessed by single crystal analysis (vide infra) and characterized by a large slipping angle (in the direction of the long molecular axis) of 66.1° for **DDTT-OBT** (**5**) versus only 47.0° and 41.3° for **DDTT-SBT** (**4**) and **DDTT-SeBT** (**1**), respectively. The corresponding E_g trends in solution (2.39 eV for **1**, 2.35 eV for **4**, 2.26 eV for **5**) and in the solid state (1.88 eV for **1**, 1.91 eV for **4**, 2.06 eV for **5**) diverge, tracking the trends in the absolute maximum absorption. Thus, the data indicates that using the large Se chalcogen in the side chain substituent promotes bandgap contraction in the solid state similarly when using it as part of the heteroaromatic ring, as seen when comparing the bandgap of thiophene derivative BTBT (≈ 3.6 eV) and selenophene derivative BSBS (≈ 3.5 eV).^[73]

The electrochemical properties of the SeBT, SBT, and OBT-based compounds were investigated using differential pulse voltammetry (DPV) in *o*-C₆H₄Cl₂ with a 0.1 M Bu₄NPF₆ solution at 25 °C and using Fc/Fc⁺ as the internal standard. All redox data are shown in Figures S3 and S4 (Supporting Information) and are summarized in Table 1. As expected, the oxidation (E_{ox}) and reduction (E_{red}) potentials (Figures S3a and S4a, Supporting Information) of the SeBT-based compounds vary with the conjugation length of the end capping unit (+0.92/−1.69 V (**1**), +0.98/−1.75 V (**2**), +1.02/−1.88 V (**3**)), while are completely insensitive on the selenoalkyl chain length (+0.92/−1.69 V for **1**, **1B**, and **1C**). From the redox potentials of the XBTs the HOMO and LUMO energies ($E_{\text{HOMO}}/E_{\text{LUMO}}$) were estimated using known equations (see footnotes in Table 1 for calculation details).^[48] Thus, going from the **T** to the **DDTT** end-functionalization of **SeBT** molecules, the HOMO and LUMO energies [$E_{\text{HOMO}}/E_{\text{LUMO}} = -5.22/-2.32$ eV (**3**), $-5.18/-2.45$ eV (**2**), $-5.12/-2.50$ eV (**1**) (Figure S3b, Supporting Information)] are up-/downshifted by $\approx 0.1/\approx 0.18$ eV, respectively, due to energy gap contraction. These results are in line with increased π -conjugation of the organic semiconductors. Notably, the E_{HOMO} (−5.12 eV) of **DDTT-SeBT** (**1**) should provide a low energy offset for facile hole injection in OFETs devices when using Au as electrode material.^[49] For comparison, the oxidation/reduction potentials of thioalkyl-substituted **DDTT-SBT** (**4**)^[47] are +0.87/−1.62 V and thus the derived $E_{\text{HOMO}}/E_{\text{LUMO}}$ are found to be $-5.07/-2.58$ eV. The alkoxy-substituted **DDTT-OBT** (**5**) exhibits the lowest oxidation potential around +0.59 V and cannot be reduced, in agreement with the great electron-donating capacity of alkoxy substituents. Note, E_{ox} of **5** is even slightly lower than that of the ferrocene internal standard, and this result was further confirmed by control experiments carried out without ferrocene (Figure S4b, Supporting Information) and by mixing molecules **1** and **5** (Figure S4c, Supporting Information). Thus, the derived E_{HOMO} of **5** is estimated at -4.79 eV, which should result in an easily p-dopable semiconductor.^[58] Thus this data, which are recorded in solution, suggests that

-SR and -SeR minimally affects the HOMO energies while the LUMO energies are more affected; on the contrary -OR strongly affects both molecular orbital energetics. Note, to access the stability of the redox processes and oxidized species, we carried out cyclic voltammetry experiments for the compounds **DDTT-SeBT** (**1**), **DDTT-SBT** (**4**), and **DDTT-OBT** (**5**) (Figure S5, Supporting Information). The data demonstrate (quasi)reversible oxidations and that compounds **1** and **4** are comparatively more stable than **5**.

Finally, the backbone geometries, energy levels, and frontier molecular orbital topologies of molecules **1–5** were studied by density functional theory (DFT) calculations at B3LYP/6-31* level (Figure 4a,b; Figure S6a,b, Supporting Information). The selenoalkyl, thioalkyl, and alkoxy side chains were replaced with selenomethyl, thiomethyl, and ethoxy groups to simplify the calculations.

DFT computations indicate that the frontier molecular orbital topologies are typical of that of catenated-fused thiophenes with an aromatic HOMO and a quinoid LUMO topologies. The gas-phase computed energy levels also track that found experimentally from solution electrochemistry. More importantly we found that the computed skeletal torsion of the SeBT unit in **1–3** (Figure S6, Supporting Information) was found to be 0.14° – 0.18° with short Se...S intramolecular distance of ≈ 3.15 Å. The computed torsions of **1–3** are smaller/close to those of **DDTT-SBT** (**4**) (4.7°) and **DDTT-OBT** (**5**) (0.17°) compounds, data confirmed from single crystal structure analysis (vide infra). This result is remarkable since gas-phase computations typically overestimate torsions found in the solid state when intermolecular forces tend to planarize π -conjugated molecules.^[94] Thus, these computations strongly suggest that intramolecular lock is very effective within the whole chalcogen series. Furthermore, the data indicates that backbone distortions from planarity in these molecules occurs only between the central XBT core and the end-capping DTT, DT, and T units, with torsions varying from 13.5° to 15.9° . Thus, overall substantial core planarity and widely delocalized FMO topologies indicate that all semiconductors have a suitable electronic structure for efficient charge transport.^[95–97]

2.3. Single Crystal Structure

Single crystals of **1**, **1B**, **4**, and **5** molecules were obtained by slow solvent evaporation from hexanes and dichloromethane solvent mixture. The relevant crystallographic data of SeBT compounds **1** and **1B** are summarized in Tables S1 and S2, respectively. Molecules **1** (Figure 5a; Figure S7, Supporting Information) and **1B** (Figure S8, Supporting Information) crystallize in a triclinic *P*-1 space group with both selenoalkyl chains are located on the opposite core face. The intramolecular distances between Se(alkyl)...S(thio) are only ≈ 3.15 Å for both molecules. These distances are well below the sum of the van der Waals radii of Se and S atoms (≈ 3.70 Å), which suggests that the Se(R) and S(Thio) atoms are locked through strong intramolecular interactions. Importantly, the torsion between the two thiophenes in the central SeBT core for both is 0.0° , resulting in a completely planar structure. The two end-capped DTT units are also almost coplanar to the central SeBT core with small torsional angles of

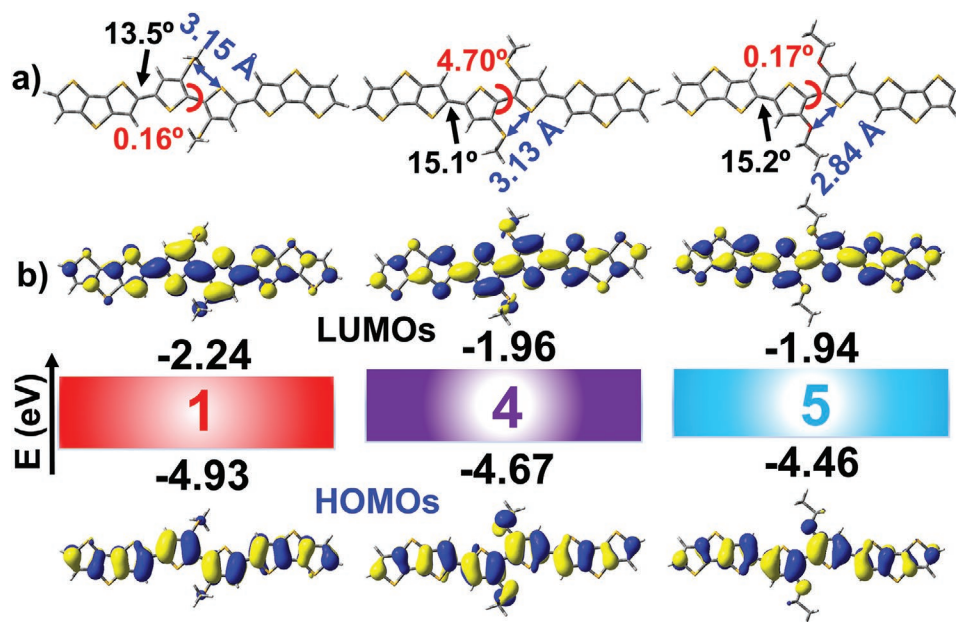


Figure 4. a) DFT/B3LYP geometry and b) HOMO/LUMO molecular orbital contours and energy levels of compounds 1, 4, and 5. Note, B3LYP is known to overestimate conjugation and torsional barriers.

7.9° (1) and 8.0° (1B). This result is in complete agreement with gas-phase DFT computations. The shortest face-to-face intermolecular planar distance between two molecules is 3.50 Å for both compounds. The two C14 and C10 alkyl chains on 1 and 1B, respectively, are located on the opposite core face (Figure 5a; Figures S7b and S8a–c, Supporting Information). Compounds 1 and 1B stack in a brick type molecular packing with a slipping angle of 41.3° and 41.4°, respectively, in the direction of the long molecular axis (Figures S7c and S8d, Supporting Information) and 74.1° and 74.0°, respectively, in the direction of the short molecular axis (Figures S7f and S8g, Supporting Information). Further, front view and top view stacked molecular arrangements are given in Figures S7d,e and S8e,f of the Supporting

Information. These data indicate that chain length variations have minimal effect of major core and stacking structural parameters and the presence of very planar molecular cores at short packing distances in both compounds suggests favorable intra- and intermolecular π - π orbital interactions which, in absence of major morphological defects, should promote charge transport.

To understand the structural effect of chalcogen in the substituent the crystal structures of both DDTT-SBT (4) and DDTT-OBT (5) were accessed. Note, although we reported the synthesis of DDTT-SBT (4) previously, we were unable to obtain single crystals. Molecule DDTT-SBT (4) (Figure 5b; Figure S9 and Table S3, Supporting Information) crystallizes in a triclinic *P1* space group and exhibits a short intramolecular distance

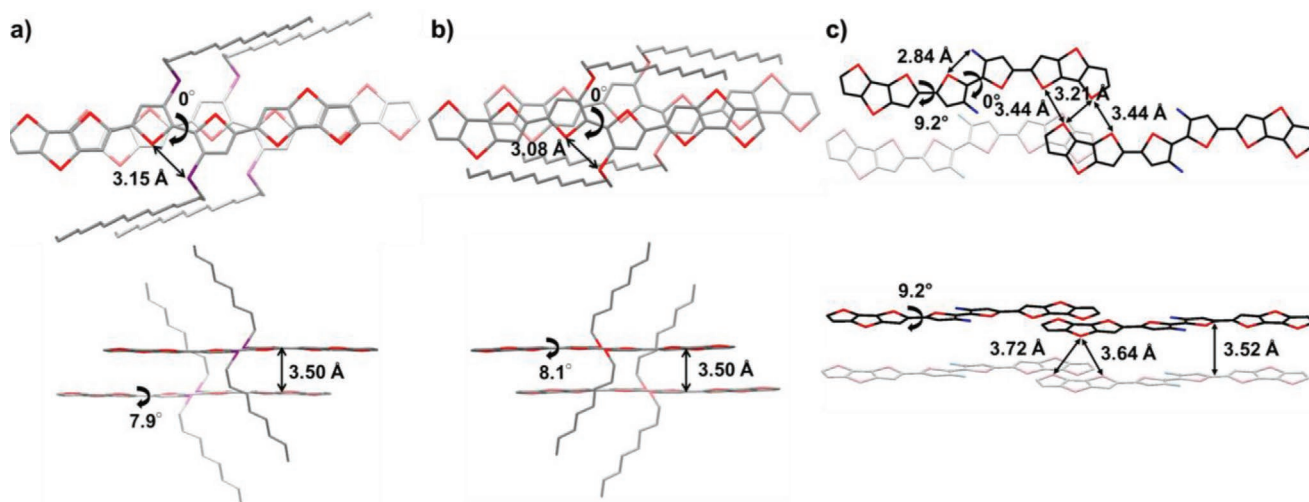


Figure 5. Single crystal structures of a) DDTT-SeBT (1), b) DDTT-SBT (4), and c) DDTT-OBT (5). The selenium, sulfur, and oxygen atoms are specified in purple, red, and blue color, respectively. The alkyl chains are omitted for clarity.

between S(alkyl)⋯S(thio) of only ≈ 3.08 Å, corroborating the existence of an intramolecular nonbonded interaction between two sulfur atoms. These distances are well below the sum of the van der Waals radii of two S atoms (≈ 3.60 Å). Similar to the SeBT unit, the torsion between the two thiophenes in the central SBT core is 0.0° , resulting in a completely planar core structure. The two end-capped DTT units are attached to the central SBT core with small torsional angles of 8.1° , which is slightly larger than in **DDTT-SeBT** (**1**) (Figure 5b). The shortest face-to-face intermolecular planar distance for molecule **4** is 3.50 Å, which is identical to that in **DDTT-SeBT** (**1**) (Figure 5b; Figure S9a, Supporting Information). Like the alkyl chains in **DDTT-SeBT** (**1**), the two C14 alkyl chains of **4** are located on the opposite core plane. Compound **4** stacks in a brick type molecular packing with a slipping angle of 47.0° in the direction of the long molecular axis (Figure S9b, Supporting Information) and 73.1° in the direction of the short molecular axis (Figure S9e, Supporting Information). Further, molecular arrangements are given in Figure S9c,d of the Supporting Information. The structure and intramolecular parameters are consistent with the large carrier mobility previously measured for this compound,^[47] and now better rationalized.

The single crystals of the new compound **DDTT-OBT** (**5**), which were also obtained by slow solvent evaporation from a dichloromethane and hexanes solvent mixture (Figure 5c; Figure S10 and Table S4, Supporting Information) exhibit a triclinic *P*-1 space group. Note, unlike in **DDTT-SeBT** (**1**) and **DDTT-SBT** (**4**), the thiophenes connecting the central OBT and the end-capping DTT units are in a *syn*-conformation in **DDTT-OBT** (**5**) and the two -OC14 chains on **DDTT-OBT** (**5**) are located in the same plane of the central OBT core (Figure S10e,f, Supporting Information). As shown in Figure 5c, the intramolecular O(alkyl)⋯S(thio) distances in the central OBT core are ≈ 2.84 Å, again shorter than the sum of the van der Waals radii of O and S atoms (≈ 3.32 Å) and demonstrating intramolecular lock. The torsion between the two thiophenes in the central OBT core is also 0.0° . Note, among the same packing layer, two adjacent end-capped DTTs in two neighboring OBT molecules exhibit short intermolecular S⋯S distances of only 3.21 Å and 3.44 Å (Figure S10g, Supporting Information). Thus, OBT molecules are connected in a zig-zag arrangement via the assistance of S⋯S interactions between the end-capping DTTs (Figure S10a,b, Supporting Information). As depicted in Figure 5c, the interplanar distances of two OBT molecules are ≈ 3.52 Å and the dihedral angles between OBT central core and the DTT units are 9.2° , which is larger than those of in SeBT (7.9°), evidencing OBT molecule is more twisted than SeBT. Furthermore, the connecting angle of the end-capped DTTs to the central OBT core is quite large around 33.9° (Figure S10c, Supporting Information). By contrast, end-capped DTTs in **DDTT-SeBT** (**1**) are connecting in a more linear arrangement to the central SeBT core, with connecting angle of 10.4° (Figure S10d, Supporting Information). Among the same columnar stack, the distances of S(upper layer)⋯S(bottom layer) in two vertical DTTs are 3.64 and 3.72 Å (Figure 5c), indicating no obvious interlayer S⋯S interactions among the OBT columnar piles. Finally, OBT molecules stack in a brick-type molecular packing with a slipping angle of 66.1° in the direction of the long molecular axis (Figure S10h, Supporting Information) and a

slipping angle of 34.9° in the direction of the short molecular axis (Figure S10i, Supporting Information). Thus, the more twisted and bended molecular structure and the poorer cofacial molecular stacking arrangement in **DDTT-OBT** (**5**) result in a packing less favorable for efficient for charge transport (vide infra).

A summary of key intramolecular lock parameters for **1**, **4**, and **5** are collected in Figure 5a–c. From the crystal data it is clear that chalcogen atom variation does not affect molecular core conformation. Importantly, intramolecular chalcogen (X)⋯S(thiophene) distance were found to be 3.15 Å for Se⋯S in **1**, 3.08 Å for S⋯S in **4**, and 2.84 Å for O⋯S in **5**. These values are well-below those of the sum of the van der Waals radii of the corresponding atoms (O and S (3.32 Å), S and S (3.60 Å) and, Se and S (3.70 Å)), thus intramolecular lock is very effective along the whole series. Interestingly, the calculated X⋯S distance compression achieved in this series due to intramolecular locks are found to increase in the order of O⋯S (14.2%) < S⋯S (14.8%) < Se⋯S (14.9%), thus the lock appears to even strengthen with the larger chalcogen. This result translates in SeBT, SBT, and OBT units that are completely planar with an inter-ring torsion of 0.0° in all cases. These data are in good agreement with the computations and demonstrate the efficacy of Se⋯S intramolecular lock in rigidifying and planarizing the BT unit, thus the SeBT can be used as a building block for constructing well-conjugated organic semiconductors.

2.4. Charge Transport in FETs

The charge transport properties of all new semiconductors were investigated by fabricating and characterizing OFETs with a bottom-gate top-contact configuration (details in the Supporting Information). OFETs were fabricated by solution-shearing organic semiconductor solutions ($4\text{--}6$ mg mL⁻¹) in chlorobenzene on PETS-modified Si/(300 nm)SiO₂ (gate contact/gate dielectric) substrates (see details in the Experimental Section of the Supporting Information).

Semiconductor thicknesses are $70\text{--}90$ nm as accessed by surface profiler. Next, the as-prepared films were dried at 70 °C (except for **2** and **3**, at room temperature, considering the very low T_m) for 2 h under vacuum and device fabrication was completed by thermal evaporation of Au source/drain electrodes. Measurements, carried out in N₂, indicate that compounds **1**, **1B**, **1C**, and **5** are FET-active while both **2** and **3** are inactive. The inactive OFETs are due to the very poor film morphologies of **2** and **3**, as discussed in the next section, since their molecular orbital energetic ($E_{\text{HOMO}} \approx 5.2$ eV) are reasonable for hole transport. All functioning devices exhibit clear current saturation and pinch-off behavior by an applied negative V_g , implying that all these compounds are p-type semiconductors. Representative gate voltage (V_g)–drain current (I_d) transfer (recorded in saturation; drain voltage (V_d) = -100 V) and V_d – I_d output characteristics for these OFETs are showed in Figure 6. OFETs mobilities were extracted in the saturation region using conventional fitting models^[98] and Table 2 summarizes the transistor performance parameters including maximum and average mobility (μ_{max} and μ_{avg}), threshold voltage (V_{th}) and current ON/OFF ratio ($I_{\text{ON}}/I_{\text{OFF}}$). The μ_{max} of SeBT (**1**, **1B**, and **1C**) based devices

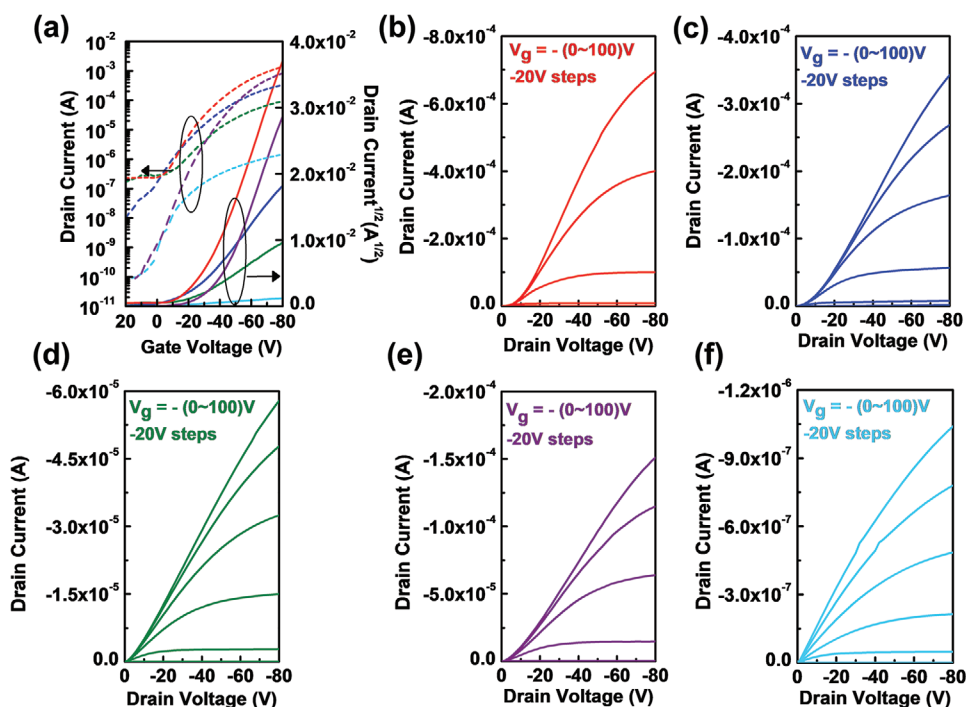


Figure 6. a) Representative OFET transfer characteristics and b–f) output characteristics of shear-coated films of: **1** (red), **1B** (blue), **1C** (green), **4** (purple), and **5** (cyan).

is 4.01, 0.60, and 0.09 $\text{cm}^2 \text{V}^{-1} \text{s}^{-1}$ while the μ_{avg} are 1.94 ± 0.90 , 0.24 ± 0.18 , and $0.03 \pm 0.02 \text{ cm}^2 \text{V}^{-1} \text{s}^{-1}$, respectively. The $I_{\text{ON}}/I_{\text{OFF}}$ of these devices are moderate to high, 10^4 – 10^6 , noting that the semiconductor channel is unpatterned. Device performance can be enhanced further by reducing the contact resistance, which is considerable in these devices, as evidenced by the output characteristics at low V_d and by patterning the semiconductor layer.^[99] The output characteristics do not show clear saturation at large gate biases because our channel length is quite small (25 μm) versus the bias we apply, resulting in short channel effects.^[100] Note, for lower biases clear saturation is seen. This effect has been reported in the previous literatures.^[101,102] However, this effect can be suppressed by tuning the Schottky barriers,^[103] active layer thickness,^[104] dielectric thickness,^[105] and enlarged channel length.^[106] Thus, from these data, variation of alkyl chain length tunes charge transport primarily by affecting the sheared film morphology and microstructure (see also GIXRD discussion later), considering that the molecular packing and energetic are very similar in this series.

The mobility data discussed above were obtained from charge transport parallel (μ_{\parallel}) to the semiconductor shearing direction (0°), thus in the direction of charge transport between the source and drain electrodes. Since a shearing force can induce crystal alignment and charge transport anisotropy in OFETs,^[107] the average mobility ($\mu_{\perp,\text{avg}}$) of the best semiconductor of **1** was also evaluated along the direction perpendicular to the shearing direction (90°) as well as, for comparison, in devices fabricated with isotropic spin-coated films. Thus, **1** OFETs tested in the direction perpendicular to the shearing direction exhibit a $\mu_{\perp,\text{avg}}$ $0.75 \pm 0.20 \text{ cm}^2 \text{V}^{-1} \text{s}^{-1}$. The $\approx 60\%$ mobility reduction confirms the anisotropic charge transport behavior of these devices, in agreement with the aligned semiconductor film morphology achieved by solution-shearing. As expected, OFET data of the spin coated **1** film in Figure S11a,b of the Supporting Information demonstrated a mobility of only $0.01 \text{ cm}^2 \text{V}^{-1} \text{s}^{-1}$, in line with previous results when comparing the transport data of solution-sheared versus spin-coated semiconductor films.^[30] Fast solvent evaporation results in isotropic and poorly

Table 2. OFETs performances of the indicated semiconductors and crystallographic parameters of **1-1C**, **4**, and **5** films.

Cpd ^{a)}	μ_{max} (μ_{avg}) ^{b)} [$\text{cm}^2 \text{V}^{-1} \text{s}^{-1}$]	$I_{\text{ON}}/I_{\text{OFF}}$	V_{th} ^{b)} [V]	d_{π} [\AA]	d_{back} [\AA]	d_{lam} [\AA]	FWHM ^{c)} [nm^{-1}]	L_c ^{c)} [nm]	Face on ratio [%]
1	4.01 (1.94 \pm 0.90)	10^4 – 10^6	-26.1 ± 17.6	3.78	13.3	19.2	0.07	80.8	4
1B	0.60 (0.24 \pm 0.18)	10^3 – 10^5	-19.2 ± 10.7	3.80	13.3	15.7	0.12	47.1	7
1C	0.09 (0.03 \pm 0.02)	10^2 – 10^5	-18.6 ± 6.8	3.86	13.3	13.7	0.19	29.8	13
4 ^{a)}	1.70 (1.00 \pm 0.30)	10^4 – 10^6	-38.0 ± 13.0	4.90	13.4	18.4	0.28	20.2	8
5	9.32×10^{-4} ($(3.31 \pm 2.38) \times 10^{-4}$)	10^3 – 10^4	2.43 ± 5.3	–	–	21.6	0.44	12.9	21

^{a)} For **4** from ref. [47]; ^{b)} Average of at least 10 devices parallel to the shearing direction (μ_{\parallel}); ^{c)} Obtained from the (001) reflection.

organized films (see morphological imaging in Figure S11c,d, Supporting Information). Thus, solution-shearing substantially improves the crystallinity of **1** film, as compared with those in the spin-coated films, enhancing mobility and generating charge transport anisotropy. When moving from DDTT-SeBT (**1**) devices to those based on the corresponding DDTT-SBT (**4**) and DDTT-OBT (**5**) semiconductors, the effect of the chalcogen in the substituent on charge transport can be quantified. As seen from Table 2, $\mu_{\max}/\mu_{\text{avg}}$ reduces going from **1** (4.01/1.94 cm² V⁻¹ s⁻¹) to **4** (1.70/1.00 cm² V⁻¹ s⁻¹), but more dramatically to **5** ($\approx 0.001/3 \times 10^{-4}$ cm² V⁻¹ s⁻¹), demonstrating that selenium incorporation in the substituent is the most effective in the chalcogen series to enhance carrier mobility. The mobility depression seen here ($\approx 2\text{--}3\times$ lower for -SR vs -SeR, $\approx 1000\times$ lower for -OR vs -SR) are in line with those measured when comparing vis-a-vis selenophene-based versus thiophene-based versus furane-based OFET semiconductors.^[73,89,90] Therefore, selenoalkyl functionalization of thiophene-based structures is equally benign, but with lower cost impact, as replacing thiophene with selenophene for designing high performance organic semiconductors.

2.5. Film Morphological Analysis

We have accessed the film morphology of **1–5** films fabricated in the same conditions, and using the same substrates, employed for FET measurements. Thus, films were deposited by the solution-shearing method on PETS-treated Si/SiO₂ substrates (see details later and in the Supporting Information) and the samples were characterized by polarized optical microscope (POM) and AFM. POM images in Figure 7a,b demonstrate that SeBT-based **1** and **1B** films are highly textured, continuous, and unidirectionally aligned along the shearing direction. The similar color between the neighboring crystalline domains in **1** and **1B** demonstrate good film uniformity and molecular alignment across grain boundaries.^[108,109] By contrast, significant color variations between the crystalline domains are observed for **1C** film (Figure 7c), which implies nonuniformity in both molecular orientation and thickness of the grains. We mainly attribute this result to fast crystallization of compound **1C** due to its poor solubility as the consequence of the short side chain, thus, the limited time for **1C** molecules to migrate to crystal seeds and form large domains during the shearing process. Figure S12 of the Supporting Information shows the AFM topographical images of **1**, **1B**, and **1C** films obtained by solution-shearing process. For all selenoalkyl-based films long and rod-shaped grains are observed evidencing a layer-by-layer stacked crystal morphology. Densely packed microcrystals can be found for **1** and **1B** films, which can thus create continuous charge transport pathways, however, **1C** films exhibit large gaps between micro-sized domains and the step height (or thickness) of the crystal is as high as 75 nm (see inset of Figure S12c, Supporting Information), which may act as charge trap as seen for other highly textured, but disconnected, semiconductor films integrated in OFETs.^[110,111] Interestingly, the film morphologies of both compounds **2** and **3** are also nonoptimal and unfavorable for high-performance OFETs. Thus, the solution-sheared **2** film appears amorphous and smooth in the continuous areas with

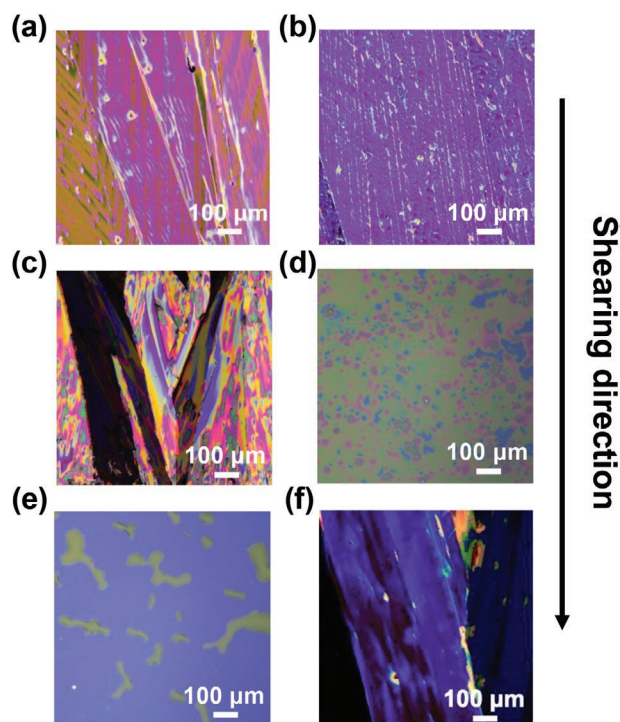


Figure 7. POM images of solution-sheared a) **1**, b) **1B**, c) **1C**, d) **2**, e) **3**, and f) **5** films along the direction indicated by the arrow on the right of the figure.

scattered isotropic holes (Figure 7d). Similarly, compound **3** film has an amorphous morphology exhibiting completely discontinuous island-like rounded features (Figure 7e). The poor morphologies of **2** and **3** films are likely the result of the very low T_m of these two compounds even though, note, their films were solution-sheared at room temperature.

The effect of chalcogen atom on the thin film morphology was also investigated. POM images of DDTT-SBT (**4**)^[47] as well as for DDTT-OBT (**5**) (Figure 7f) films reveals formation of large and macroscopically aligned crystals when processed under the same shearing process conditions. However, AFM images reveal subtle differences. Thus, ≈ 5 μm wide rod-like flat crystallites are observed for both compounds **1** (Figure S12a, Supporting Information) and **4**^[47] films, implying strong molecular aggregation imparting considerable crystallinity. However, compound **5** film consists of similar rod-like features but having irregular contours and overlaid with much smaller and randomly oriented aggregates (Figure S12d, Supporting Information). This type of mixed morphological features may not favor device performance.^[112] These morphological variations imply that S and Se substitution in the SBT and SeBT central core can significantly improve formation of ordered and oriented aggregates, which can originate from the more diffuse electron density and larger polarizabilities of S and Se compared to the lighter O atom.^[55]

2.6. Thin Film Microstructural Analysis

The microstructure and molecular ordering of all new DTT end-capped compounds films were investigated by 2D GIXRD

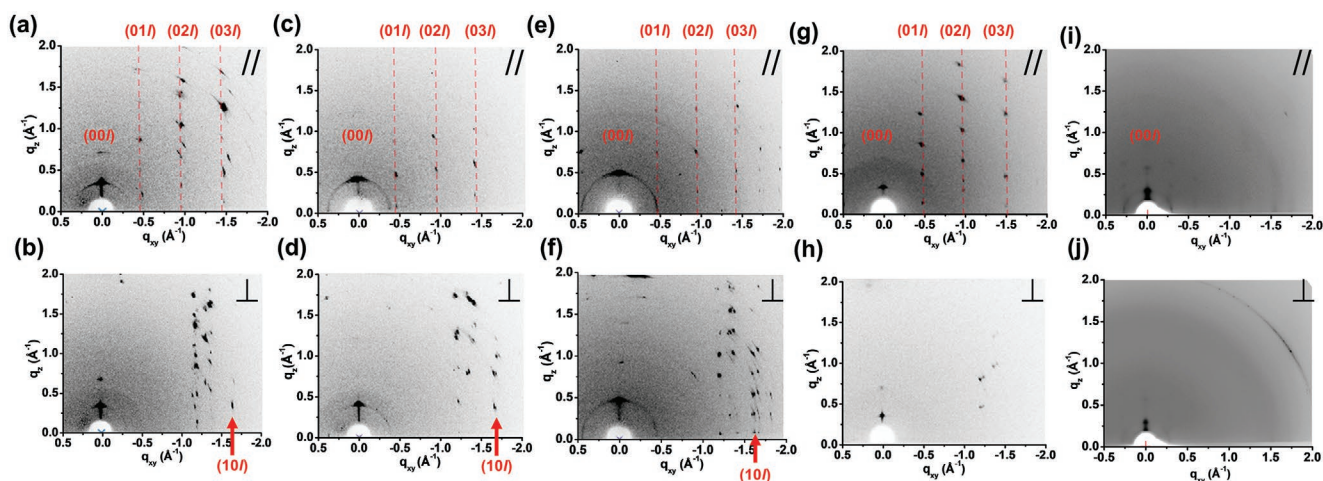


Figure 8. 2D GIXRD patterns of solution-sheared thin films: a,b) **1**, c,d) **1B**, e,f) **1C**, g,h) **4**, and i,j) **5**. The patterns were recorded for the incident X-ray beam oriented (a,c,e,g,i) parallel and (b,d,f,h,j) perpendicular to the shearing direction.

using a high-resolution synchrotron X-ray source. Sample films were prepared under conditions identical to those of OFET fabrication. The 2D patterns with the grazing incident X-ray beam parallel and perpendicular to the shearing direction are shown in **Figure 8** and the resulting crystallographic spacings (d 's) are summarized in Table 2, where d_{π} , d_{back} , and d_{lam} are the periodicities along the π -stacking, molecular backbone, and lamellar directions, respectively. The orientation of the molecular packing under the shearing process can be determined by comparing the diffraction patterns along and across the shearing direction. It is known that the shearing process can efficiently orient organic semiconductor molecules in thin films.^[30,32,47–49] First, **Figure 8** points that all **1**, **1B**, and **1C** films exhibit (00l) reflections in the out-of-plane direction, which results from the periodic stacking of the selenotetradecyl side chains and molecular backbone along the film thickness. Sharp Bragg spots progressing up to (002) are seen for **1**, corresponding to a d_{lam} of 19.2 Å (determined from (001) at $q_z = 0.33 \text{ \AA}^{-1}$). **1B** and **1C** films show only one arc in the out-of-plane direction centered at $q_z = 0.40$ and 0.46 \AA^{-1} , corresponding to d_{lam} of 15.7 and 13.7 Å, respectively, indicating a less order lamellar stacking than that of **1** film. The (00l) spacings of DDTT-SeBTs follow the lengths of the side chains, but they are shorter than the full extended selenoalkyl side chains, suggesting that the side chains pack in an interdigitated and tilted fashion (**Figure 9**).

The (10l) reflections associated with the molecular core π -stacking (indicated by the red arrows in the perpendicular patterns) are located at $q_{xy} = 1.66$, 1.65, and 1.63 \AA^{-1} for **1**, **1B**, and **1C**, respectively, evidencing the smallest d_{π} of 3.78 Å for compound **1**, followed by **1B** (3.80 Å) and **1C** (3.86 Å). In addition, strong diffraction patterns assignable to the (01l), (02l), and (03l) reflections, associated to backbone periodicities ($d_{\text{back}} = 1$ (13.3 Å), **1B** (13.3 Å), and **1C** (13.3 Å)), are observed for beam scan in the direction parallel to the shearing coating while the (10l) reflection is detected when the beam is pointed perpendicular to the shearing direction. The different patterns indicate that solution-shearing can align these molecules as the optical images of the crystal suggested (vide supra). When comparing the three chalcogenoalkyl-substituted **1**, **4**, and **5**

compounds, all compounds exhibit at least one (00l) lamellar diffraction and the corresponding d_{lam} of **5** is found to be considerably lengthened to 21.6 Å as compared to 18.4 and 19.2 Å for **4** and **1**, respectively. This is the result of the more stretched alkoxy side chains of compound **5**, in agreement with single crystal analysis (Figure S10, Supporting Information). In addition, compound **5** exhibits only weak diffractions and lacks scattering from the π - π stacking, indicative of the significantly reduced crystallinity of this compound, corroborating poor charge transport characteristics. Unlike **5**, the larger -SR and -SeR containing molecules **4** and **1** exhibit strong (00l) lamellar diffractions both in the parallel/perpendicular directions as well as (10l) π - π stacking diffractions ($d_{\pi} = 4$ (4.90 Å), and **1** (3.78 Å)) and (01l)/(02l)/(03l) diffractions in the parallel and perpendicular directions ($d_{\text{back}} = 4$ (13.4 Å), and **1** (13.3 Å)), respectively, signifying that both compounds adopt identical stacking characteristics. Overall, the crystal phase of **1** film measured by GIXRD is identical to that identified by single crystal analysis, thus the brick-stacked intermolecular arrangement is preserved going from single crystal to the polycrystalline thin film, which thus retains a supramolecular arrangement for strong electronic coupling.^[113,114] Furthermore, d_{π} seen in **1** versus **4**, maximizes intermolecular interactions, favoring transfer of charge carriers,^[115,116] again in agreement with the greatest OFET

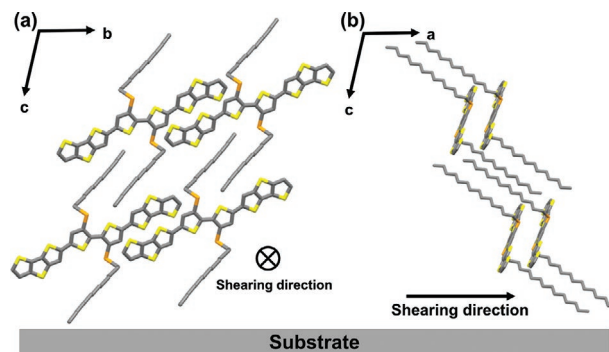


Figure 9. Schematic diagram of the molecular packing of a solution-sheared **1** film in the a) a -axis and b) in the b -axis projections.

response. The considerable alignment of **1** film upon solution-shearing is further supported by polarized absorption spectra measurements (Figure S13a, Supporting Information). The dichroic ratio ($DR = A_{\perp}/A_{\parallel}$) of **1** film under shearing is estimated to be 2.04, where A_{\perp} and A_{\parallel} are the absorbance bands at 505 nm recorded for the incident polarized light perpendicular and parallel to the shearing direction, respectively. By contrast, a DR is ≈ 1 was measured for the spin-coated **1** film (Figure S13b, Supporting Information), indicating that the structure is isotropic in the absence of shearing. Note, a similar result was obtained for solution-sheared/spin-coated films of **4**.

The 1D diffraction data extracted from the 2D GIXRD patterns can also be used to quantify the crystallographic coherence lengths (L_c) and the crystallite orientation distributions of compounds with different selenoalkyl side chain lengths (**1** vs **1B** vs **1C**) and chalcogen atoms in the substituent (**1** vs **4** vs **5**). These data are also collected in Table 2. The full width at half-maximum (FWHM) of the diffraction peaks shown in Figure S14 of the Supporting Information provides the information on L_c that relates to the crystallite size.^[17] The FWHM of the (001) reflection is 0.07, 0.12, 0.19, 0.28, and 0.44 nm⁻¹ for **1**, **1B**, **1C**, **4**, and **5**, respectively. Through the Scherrer equation, L_c s for **1**, **1B**, **1C**, **4**, and **5** are calculated to be 80.8, 471, 29.8, 20.2, and 12.9 nm, respectively. These results demonstrate that the order along the selenoalkyl direction noticeably decreases with decreasing the side chain length. Similarly, when moving from -SeR to -SR to -OR in **1** to **4** to **5**, respectively, L_c dramatically decreases, in line with the greater molecular packing characteristics of the heavy chalcogen functionalized molecule and the highest mobility obtained in compound **1**. The crystallite orientation was quantitatively determined by the intensity distribution over the azimuthal angle (χ) of the (001) diffraction, as shown in Figure S15 of the Supporting Information. The area between $\chi = 45^\circ$ and 135° represents the edge-on oriented molecule population while those between $\chi = 0^\circ$ to 45° and 135° to 180° are the face-on oriented molecular population. Thus, the face-on fraction increases from 4% for **1** to 7% for **1B** and to 13% for **1C** as the selenoalkyl side chain length decreases and, similarly, when moving from the larger to the smaller chalcogen (4% for **1** to 8% for **4** and to 21% for **5**).

Based on the GIXRD data, and further supported by polarized absorption spectra, the molecular arrangement in the solution-sheared thin films of **1**–**5** versus both the shearing direction the dielectric surface can be accessed and is pictorially reported in Figure 10.

The appearance of the (00 l) and the (10 l) peaks in the out-of-plane and in-plane directions, respectively, suggests a preferential edge-on arrangement of **1**'s molecules. Furthermore, the fact that the (10 l) peaks appear only in the perpendicular GIXRD pattern indicates the π -stacking is along the shearing direction. Since the transition dipole lies perpendicular to the conjugated backbone, the high DR of the sheared **1** film shown in Figure S13a of the Supporting Information implies that the long axis of the backbones are aligned perpendicular to the shearing direction,^[118] a data consistent with the GIXRD results. Similar morphological evolutions can be drawn for the other semiconductors, however, with the crystals less aligned and with a progressively increased face-on population upon shortening the substituent and reducing the chalcogen size. The

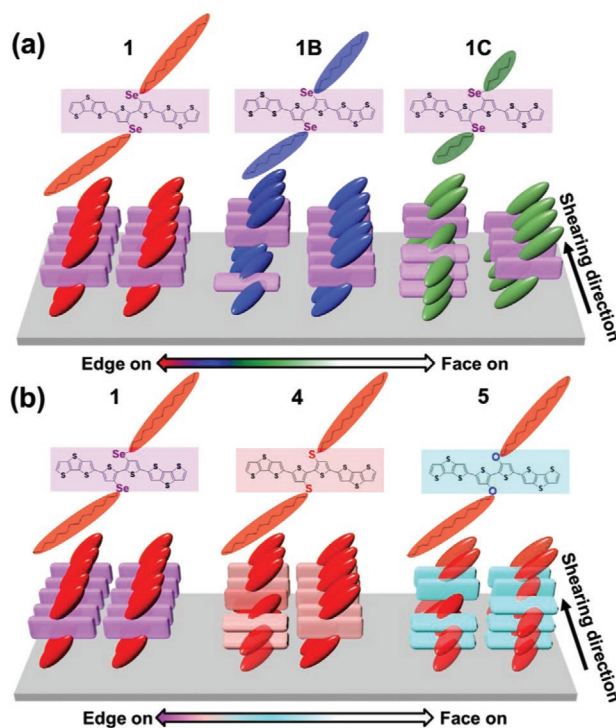


Figure 10. Illustration of the molecular orientation of the indicated films pointing to a transition from an exclusively edge-on molecular orientation in **1** to mixed edge-on/face-on orientations.

combined analyses demonstrate not only that solution-sheared films of **1** are the most textured but exhibits the most favorable π -stacking oriented crystallites at the shortest distance thus corroborating, in combination with the microscopic film morphology, the superior charge transport of the corresponding OFETs versus those of the other compounds.

3. Conclusions

In conclusion, six new organic semiconductors were developed, and charge transport assessed in solution-sheared OFETs. Single crystal structures of SeBT (**1** and **1B**), SBT (**4**), and OBT (**5**) based compounds were solved demonstrating that intramolecular lock is not only preserved along the whole chalcogenated molecular series, but it even intensifies for the larger Se atom, affording highly planar and π -conjugated XBT-based molecular structures. While structure and energetic of all compounds synthesized here are reasonable for hole conduction, the morphology of the solution-sheared films strongly dominates OFET performance as rationalized by a combination of macro/microscopic film morphology, film texturing, and orientation phase purity of the corresponding films. Among these, compound **1** exhibits a maximum carrier mobility of 4.01 cm² V⁻¹ s⁻¹, which is the greatest in this series and the largest hole transporting value reported to date for all fused-thiophene-based organic small molecular semiconductors. When comparing vis-à-vis the chalcogen effect, the carrier mobility decreases steadily when moving to sulfur (1.70 cm² V⁻¹ s⁻¹ for **4**) and to oxygen (9.32 × 10⁻⁴ cm² V⁻¹ s⁻¹

for 5) containing substituents. Our data demonstrate for the first time that, from a charge transport perspective, employing a chalcogen as part of a substituent of a π -conjugated core is equivalent of using it as internal part of a heteroaromatic ring. Thus, our findings provide a new viewpoint to investigate the structure–property relationship of organic semiconductors and suggest a new route toward rationally designed solution processable high performance semiconducting materials.

Supporting Information

Supporting Information is available from the Wiley Online Library or from the author.

Acknowledgements

S.N.A. and C.-C.L. contributed equally to this work. M.-C.C. thanks the financial support provided by the Ministry of Science and Technology (MOST) of Taiwan (MOST-109-3111-8-008-001 and MOST-110-2628-8-008-007) and NCU-Covestro Research Center. C.-L.L. thanks to Young Scholar Fellowship Program (Columbus Program) by MOST in Taiwan (MOST-110-2636-E-002-021). A.F. thanks the AFOSR (Grant No. FA9550-18-1-0320). The authors thank Beamline B13A1/B17A1/B23A1 from the National Synchrotron Radiation Research Center (NSRRC) of Taiwan for providing beamtime.

Conflict of Interest

The authors declare no conflict of interest.

Data Availability Statement

Research data are not shared.

Keywords

chalcogen, dithienothiophene, high-performance, organic field effect transistors, selenoalkylated bithiophene, solution processable

Received: January 21, 2022

Revised: February 27, 2022

Published online: March 31, 2022

- [1] X. G. Guo, A. Facchetti, T. J. Marks, *Chem. Rev.* **2014**, *114*, 8943.
 [2] I. Osaka, K. Takimiya, *Adv. Mater.* **2017**, *29*, 1605218.
 [3] Y. Wang, H. Guo, A. Harbuzaru, M. A. Uddin, I. Arrechea-Marcos, S. Ling, J. Yu, Y. Tang, H. Sun, J. T. López Navarrete, R. P. Ortiz, H. Y. Woo, X. Guo, *J. Am. Chem. Soc.* **2018**, *140*, 6095.
 [4] Y. Wang, H. Guo, S. Ling, I. Arrechea-Marcos, Y. Wang, J. T. López Navarrete, R. P. Ortiz, X. Guo, *Angew. Chem., Int. Ed.* **2017**, *56*, 9924.
 [5] P. W. M. Blom, *Adv. Mater. Technol.* **2020**, *5*, 2000144.
 [6] M. Ashizawa, Y. Zheng, H. Tran, Z. Bao, *Prog. Polym. Sci.* **2020**, *100*, 101181.
 [7] N. Wang, A. Yang, Y. Fu, Y. Li, F. Yan, *Acc. Chem. Res.* **2019**, *52*, 277.
 [8] D. Khim, A. Luzio, G. E. Bonaccini, G. Pace, M.-J. Lee, Y.-Y. Noh, M. Caironi, *Adv. Mater.* **2018**, *30*, 1705463.
 [9] Q. Liu, S. E. Bottle, P. Sonar, *Adv. Mater.* **2020**, *32*, 1903882.
 [10] Y. Ren, X. Yang, L. Zhou, J.-Y. Mao, S.-T. Han, Y. Zhou, *Adv. Funct. Mater.* **2019**, *29*, 1902105.
 [11] H. Li, W. Shi, J. Song, H.-J. Jang, J. Dailey, J. Yu, H. E. Katz, *Chem. Rev.* **2019**, *119*, 3.
 [12] T. Mikie, I. Osaka, *J. Mater. Chem. C* **2020**, *8*, 14262.
 [13] G. H. Lee, H. Moon, H. Kim, G. H. Lee, W. Kwon, S. Yoo, D. Myung, S. H. Yun, Z. Bao, S. K. Hahn, *Nat. Rev. Mater.* **2020**, *5*, 149.
 [14] Y. Shi, H. Guo, J. Huang, X. Zhang, Z. Wu, K. Yang, Y. Zhang, K. Feng, H. Y. Woo, R. P. Ortiz, M. Zhou, X. Guo, *Angew. Chem., Int. Ed.* **2020**, *59*, 14449.
 [15] H. Sun, J. Gerasimov, M. Berggren, S. Fabiano, *J. Mater. Chem. C* **2018**, *6*, 11778.
 [16] C. McDowell, M. Abdelsamie, M. F. Toney, G. C. Bazan, *Adv. Mater.* **2018**, *30*, 1707114.
 [17] S. Dai, Y. Zhao, Y. Wang, J. Zhang, L. Fang, S. Jin, Y. Shao, J. Huang, *Adv. Funct. Mater.* **2019**, *29*, 1903700.
 [18] J. Yang, Z. Zhao, S. Wang, Y. Guo, Y. Liu, *Chem* **2018**, *4*, 2748.
 [19] J. Zhang, H. S. Tan, X. Guo, A. Facchetti, H. Yan, *Nat. Energy* **2018**, *3*, 720.
 [20] H. Bronstein, C. B. Nielsen, B. C. Schroeder, I. McCulloch, *Nat. Rev. Chem.* **2020**, *4*, 66.
 [21] J. Xu, H.-C. Wu, C. Zhu, A. Ehrlich, L. Shaw, M. Nikolka, S. Wang, F. Molina-Lopez, X. Gu, S. Luo, D. Zhou, Y.-H. Kim, G.-J. N. Wang, K. Gu, V. R. Feig, S. Chen, Y. Kim, T. Katsumata, Y.-Q. Zheng, H. Yan, J. W. Chung, J. Lopez, B. Murmann, Z. Bao, *Nat. Mater.* **2019**, *18*, 594.
 [22] C. Wang, W.-Y. Lee, R. Nakajima, J. Mei, D. H. Kim, Z. Bao, *Chem. Mater.* **2013**, *25*, 4806.
 [23] V. Vohra, K. Kawashima, T. Kakara, T. Koganezawa, I. Osaka, K. Takimiya, H. Murata, *Nat. Photonics* **2015**, *9*, 403.
 [24] M. Saito, T. Fukuhara, S. Kamimura, H. Ichikawa, H. Yoshida, T. Koganezawa, Y. Ie, Y. Tamai, H. D. Kim, H. Ohkita, I. Osaka, *Adv. Energy Mater.* **2020**, *10*, 1903278.
 [25] D. Kiefer, R. Kroon, A. I. Hofmann, H. Sun, X. Liu, A. Giovannitti, D. Stegerer, A. Cano, J. Hynynen, L. Yu, Y. Zhang, D. Nai, T. F. Harrelson, M. Sommer, A. J. Moulé, M. Kemerink, S. R. Marder, I. McCulloch, M. Fahlman, S. Fabiano, C. Müller, *Nat. Mater.* **2019**, *18*, 149.
 [26] H. Li, J. Wu, K. Takahashi, J. Ren, R. Wu, H. Cai, J. Wang, H. L. Xin, Q. Miao, H. Yamada, H. Chen, H. Li, *J. Am. Chem. Soc.* **2019**, *141*, 10007.
 [27] X. Guo, R. P. Ortiz, Y. Zheng, M.-G. Kim, S. Zhang, Y. Hu, G. Lu, A. Facchetti, T. J. Marks, *J. Am. Chem. Soc.* **2011**, *133*, 13685.
 [28] A. Liu, H. Zhu, W.-T. Park, S.-J. Kang, Y. Xu, M.-G. Kim, Y.-Y. Noh, *Adv. Mater.* **2018**, *30*, 1802379.
 [29] C. K. Frederickson, B. D. Rose, M. M. Haley, *Acc. Chem. Res.* **2017**, *50*, 977.
 [30] S. Vegiraju, G.-Y. He, C. Kim, P. Priyanka, Y.-J. Chiu, C.-W. Liu, C.-Y. Huang, J.-S. Ni, Y.-W. Wu, Z. Chen, G.-H. Lee, S.-H. Tung, C.-L. Liu, M.-C. Chen, A. Facchetti, *Adv. Funct. Mater.* **2017**, *27*, 1606761.
 [31] N. Zhou, S. Vegiraju, X. Yu, E. F. Manley, M. R. Butler, M. J. Leonard, P. Guo, W. Zhao, Y. Hu, K. Prabakaran, R. P. H. Chang, M. A. Ratner, L. X. Chen, A. Facchetti, M.-C. Chen, T. J. Marks, *J. Mater. Chem. C* **2015**, *3*, 8932.
 [32] A. Velusamy, C.-H. Yu, S. N. Afraj, C.-C. Lin, W.-Y. Lo, C.-J. Yeh, Y.-W. Wu, H.-C. Hsieh, J. Chen, G.-H. Lee, S.-H. Tung, C.-L. Liu, M.-C. Chen, A. Facchetti, *Adv. Sci.* **2020**, *8*, 2002930.
 [33] Z. Lu, C. Wang, W. Deng, M. T. Achille, J. Jie, X. Zhang, *J. Mater. Chem. C* **2020**, *8*, 9133.
 [34] Y. Wang, L. Sun, C. Wang, F. Yang, X. Ren, X. Zhang, H. Dong, W. Hu, *Chem. Soc. Rev.* **2019**, *48*, 1492.
 [35] R. Wu, B. Peng, H. Li, H. Li, *Chem. Mater.* **2021**, *33*, 19.

- [36] S. Chen, Z. Li, Y. Qiao, Y. Song, *J. Mater. Chem. C* **2021**, 9, 1126.
- [37] J. Wu, Q. Li, G. Xue, H. Chen, H. Li, *Adv. Mater.* **2017**, 29, 1606101.
- [38] S.-S. Cheng, P.-Y. Huang, M. Ramesh, H.-C. Chang, L.-M. Chen, C.-M. Yeh, C.-L. Hung, M.-C. Wu, C.-C. Liu, C. Kim, H.-C. Lin, M.-C. Chen, C.-W. Chu, *Adv. Funct. Mater.* **2014**, 24, 2057.
- [39] C. Zhang, X. Zhu, *Adv. Funct. Mater.* **2020**, 30, 2000765.
- [40] M. E. Cinar, T. Ozturk, *Chem. Rev.* **2015**, 115, 3036.
- [41] H. Usta, D. Kim, R. Ozdemir, Y. Zorlu, S. Kim, M. C. Ruiz Delgado, A. Harbuzaru, S. Kim, G. Demirel, J. Hong, Y.-G. Ha, K. Cho, A. Facchetti, M.-G. Kim, *Chem. Mater.* **2019**, 31, 5254.
- [42] C. Wang, X. Zhang, H. Dong, X. Chen, W. Hu, *Adv. Energy Mater.* **2020**, 10, 2000955.
- [43] P. Yu, Y. Zhen, H. Dong, W. Hu, *Chem* **2019**, 5, 2814.
- [44] K. Takimiya, S. Shinamura, I. Osaka, E. Miyazaki, *Adv. Mater.* **2011**, 23, 4347.
- [45] T. Okamoto, C. P. Yu, C. Mitsui, M. Yamagishi, H. Ishii, J. Takeya, *J. Am. Chem. Soc.* **2020**, 142, 9083.
- [46] S. N. Afraj, G.-Y. He, C.-Y. Lin, A. Velusamy, C.-Y. Huang, P.-S. Lin, S. Vegiraju, P.-Y. Huang, J.-S. Ni, S.-L. Yau, S.-H. Tung, T. Minari, C.-L. Liu, M.-C. Chen, *Adv. Mater. Technol.* **2021**, 6, 2001028.
- [47] S. Vegiraju, B.-C. Chang, P. Priyanka, D.-Y. Huang, K.-Y. Wu, L.-H. Li, W.-C. Chang, Y.-Y. Lai, S.-H. Hong, B.-C. Yu, C.-L. Wang, W.-J. Chang, C.-L. Liu, M.-C. Chen, A. Facchetti, *Adv. Mater.* **2017**, 29, 1702414.
- [48] S. Vegiraju, X.-L. Luo, L.-H. Li, S. N. Afraj, C. Lee, D. Zheng, H.-C. Hsieh, C.-C. Lin, S.-H. Hong, H.-C. Tsai, G.-H. Lee, S.-H. Tung, C.-L. Liu, M.-C. Chen, A. Facchetti, *Chem. Mater.* **2020**, 32, 1422.
- [49] C.-C. Lin, S. N. Afraj, A. Velusamy, P.-C. Yu, C.-H. Cho, J. Chen, Y.-H. Li, G.-H. Lee, S.-H. Tung, C.-L. Liu, M.-C. Chen, A. Facchetti, *ACS Nano* **2021**, 15, 727.
- [50] S. Vegiraju, A. A. Amelenan Torimtubeun, P.-S. Lin, H.-C. Tsai, W.-C. Lien, C.-S. Chen, G.-Y. He, C.-Y. Lin, D. Zheng, Y.-F. Huang, Y.-C. Wu, S.-L. Yau, G.-H. Lee, S.-H. Tung, C.-L. Wang, C.-L. Liu, M.-C. Chen, A. Facchetti, *ACS Appl. Mater. Interfaces* **2020**, 12, 25081.
- [51] S. Vegiraju, D.-Y. Huang, P. Priyanka, Y.-S. Li, X.-L. Luo, S.-H. Hong, J.-S. Ni, S.-H. Tung, C.-L. Wang, W.-C. Lien, S. L. Yau, C.-L. Liu, M.-C. Chen, *Chem. Commun.* **2017**, 53, 5898.
- [52] H. Chen, Y. Guo, G. Yu, Y. Zhao, J. Zhang, D. Gao, H. Liu, Y. Liu, *Adv. Mater.* **2012**, 24, 6418.
- [53] I. Osaka, R. Zhang, G. Sauvé, D.-M. Smilgies, T. Kowalewski, R. D. McCullough, *J. Am. Chem. Soc.* **2009**, 131, 2521.
- [54] C. Wang, Y. Qin, Y. Sun, Y.-S. Guan, W. Xu, D. Zhu, *ACS Appl. Mater. Interfaces* **2015**, 7, 15978.
- [55] H. Huang, L. Yang, A. Facchetti, T. J. Marks, *Chem. Rev.* **2017**, 117, 10291.
- [56] X. Guo, J. Quinn, Z. Chen, H. Usta, Y. Zheng, Y. Xia, J. W. Hennek, R. P. Ortiz, T. J. Marks, A. Facchetti, *J. Am. Chem. Soc.* **2013**, 135, 1986.
- [57] X. Guo, Q. Liao, E. F. Manley, Z. Wu, Y. Wang, W. Wang, T. Yang, Y.-E. Shin, X. Cheng, Y. Liang, L. X. Chen, K.-J. Baeg, T. J. Marks, X. Guo, *Chem. Mater.* **2016**, 28, 2449.
- [58] J. Huang, H. Guo, M. A. Uddin, J. Yu, H. Y. Woo, X. Guo, *Adv. Electron. Mater.* **2018**, 4, 1700519.
- [59] H. Wang, J. Huang, M. A. Uddin, B. Liu, P. Chen, S. Shi, Y. Tang, G. Xing, S. Zhang, H. Y. Woo, H. Guo, X. Guo, *ACS Appl. Mater. Interfaces* **2019**, 11, 10089.
- [60] Y. Liu, J. Song, Z. Bo, *Chem. Commun.* **2021**, 57, 302.
- [61] G. J. McEntee, P. J. Skabara, F. Vilela, S. Tierney, I. D. W. Samuel, S. Gambino, S. J. Coles, M. B. Hursthouse, R. W. Harrington, W. Clegg, *Chem. Mater.* **2010**, 22, 3000.
- [62] M. Turbiez, P. Frère, P. Leriche, N. Mercier, J. Roncali, *Chem. Commun.* **2005**, 1161.
- [63] M. Turbiez, N. Hergué, P. Leriche, P. Frère, *Tetrahedron Lett.* **2009**, 50, 7148.
- [64] Z. Fei, Y. Han, E. Gann, T. Hodsdon, A. S. R. Chesman, C. R. McNeill, T. D. Anthopoulos, M. Heeney, *J. Am. Chem. Soc.* **2017**, 139, 8552.
- [65] R. S. Ashraf, I. Meager, M. Nikolka, M. Kirkus, M. Planells, B. C. Schroeder, S. Holliday, M. Hurhangee, C. B. Nielsen, H. Sirringhaus, I. McCulloch, *J. Am. Chem. Soc.* **2015**, 137, 1314.
- [66] M. J. Sung, A. Luzio, W.-T. Park, R. Kim, E. Gann, F. Maddalena, G. Pace, Y. Xu, D. Natali, C. de Falco, L. Dang, C. R. McNeill, M. Caironi, Y.-Y. Noh, Y.-H. Kim, *Adv. Funct. Mater.* **2016**, 26, 4984.
- [67] I. Kang, T. K. An, J.-a. Hong, H.-J. Yun, R. Kim, D. S. Chung, C. E. Park, Y.-H. Kim, S.-K. Kwon, *Adv. Mater.* **2013**, 25, 524.
- [68] S.-Y. Jang, I.-B. Kim, M. Kang, Z. Fei, E. Jung, T. McCarthy-Ward, J. Shaw, D.-H. Lim, Y.-J. Kim, S. Mathur, M. Heeney, D.-Y. Kim, *Adv. Sci.* **2019**, 6, 1900245.
- [69] T. Okamoto, M. Mitani, C. P. Yu, C. Mitsui, M. Yamagishi, H. Ishii, G. Watanabe, S. Kumagai, D. Hashizume, S. Tanaka, M. Yano, T. Kushida, H. Sato, K. Sugimoto, T. Kato, J. Takeya, *J. Am. Chem. Soc.* **2020**, 142, 14974.
- [70] T. Yamamoto, K. Takimiya, *J. Am. Chem. Soc.* **2007**, 129, 2224.
- [71] T. Okamoto, K. Kudoh, A. Wakamiya, S. Yamaguchi, *Org. Lett.* **2005**, 7, 5301.
- [72] T. Izawa, E. Miyazaki, K. Takimiya, *Chem. Mater.* **2009**, 21, 903.
- [73] C. Wang, M. Abbas, G. Wantz, K. Kawabata, K. Takimiya, *J. Mater. Chem. C* **2020**, 8, 15119.
- [74] H.-J. Yun, S.-J. Kang, Y. Xu, S. O. Kim, Y.-H. Kim, Y.-Y. Noh, S.-K. Kwon, *Adv. Mater.* **2014**, 26, 7300.
- [75] A. Liu, H. Zhu, W.-T. Park, S.-J. Kim, H. Kim, M.-G. Kim, Y.-Y. Noh, *Nat. Commun.* **2020**, 11, 4309.
- [76] H. Huang, Z. Chen, R. P. Ortiz, C. Newman, H. Usta, S. Lou, J. Youn, Y.-Y. Noh, K.-J. Baeg, L. X. Chen, A. Facchetti, T. Marks, *J. Am. Chem. Soc.* **2012**, 134, 10966.
- [77] M. Nakano, H. Mori, S. Shinamura, K. Takimiya, *Chem. Mater.* **2012**, 24, 190.
- [78] H. Takenaka, T. Ogaki, C. Wang, K. Kawabata, K. Takimiya, *Chem. Mater.* **2019**, 31, 6696.
- [79] M. Al-Hashimi, Y. Han, J. Smith, H. S. Bazzi, S. Y. A. Alqaradawi, S. E. Watkins, T. D. Anthopoulos, M. Heeney, *Chem. Sci.* **2016**, 7, 1093.
- [80] A. J. Kronemeijer, E. Gili, M. Shahid, J. Rivnay, A. Salleo, M. Heeney, H. Sirringhaus, *Adv. Mater.* **2012**, 24, 1558.
- [81] H. Kong, D. S. Chung, I.-N. Kang, J.-H. Park, M.-J. Park, I. H. Jung, C. E. Park, H.-K. Shim, *J. Mater. Chem.* **2009**, 19, 3490.
- [82] J. G. Oh, Y. H. Ha, J.-H. Kim, S.-K. Kwon, T. K. An, Y.-H. Kim, J. Jang, *Org. Electron.* **2021**, 89, 106032.
- [83] Y.-J. Hwang, G. Ren, N. M. Murari, S. A. Jenekhe, *Macromolecules* **2012**, 45, 9056.
- [84] Y. Ezhumalai, F.-S. Lin, M.-S. Fan, K. Prabakaran, J.-S. Ni, Y.-C. Wu, G.-H. Lee, M.-C. Chen, K.-C. Ho, *ACS Appl. Mater. Interfaces* **2020**, 12, 15071.
- [85] F.-S. Lin, P. Priyanka, M.-S. Fan, S. Vegiraju, J.-S. Ni, Y.-C. Wu, Y.-H. Li, G.-H. Lee, Y. Ezhumalai, R.-J. Jeng, M.-C. Chen, K.-C. Ho, *J. Mater. Chem. C* **2020**, 8, 15322.
- [86] S. J. Evenson, S. C. Rasmussen, *Org. Lett.* **2010**, 12, 4054.
- [87] M.-C. Chen, Y.-J. Chiang, C. Kim, Y.-J. Guo, S.-Y. Chen, Y.-J. Liang, Y.-W. Huang, T.-S. Hu, G.-H. Lee, A. Facchetti, T. J. Marks, *Chem. Commun.* **2009**, 1846.
- [88] C. Kim, M.-C. Chen, Y.-J. Chiang, Y.-J. Guo, J. Youn, H. Huang, Y.-J. Liang, Y.-J. Lin, Y.-W. Huang, T.-S. Hu, G.-H. Lee, A. Facchetti, T. J. Marks, *Org. Electron.* **2010**, 11, 801.
- [89] O. Gidron, M. Bendikov, *Angew. Chem., Int. Ed.* **2014**, 53, 2546.
- [90] B. Mondal, M. Bendikov, U. Kanti Roy, *Russ. J. Gen. Chem.* **2019**, 89, 1911.

- [91] Y. S. K. Sasaki, M. Lu, Y. Yoshida, R. Azumi, Y. Ueda, *Adv. Mater. Phys. Chem.* **2013**, *3*, 185.
- [92] Z. Zhang, T. Lei, Q. Yan, J. Pei, D. Zhao, *Chem. Commun.* **2013**, 49, 2882.
- [93] J. Youn, S. Vegiraju, J. D. Emery, B. J. Leever, S. Kewalramani, S. J. Lou, S. Zhang, K. Prabakaran, Y. Ezhumalai, C. Kim, P.-Y. Huang, C. Stern, W.-C. Chang, M. J. Bedzyk, L. X. Chen, M.-C. Chen, A. Facchetti, T. J. Marks, *Adv. Electron. Mater.* **2015**, *1*, 1500098.
- [94] F. Xu, T. T. Testoff, L. Wang, X. Zhou, *Molecules* **2020**, *25*, 4478.
- [95] Z. Lin, X. Liu, W. Zhang, J. Huang, Q. Wang, K. Shi, Z. Chen, Y. Zhou, L. Wang, G. Yu, *Macromolecules* **2018**, *51*, 966.
- [96] Y. Gao, J. Bai, Y. Sui, Y. Han, Y. Deng, H. Tian, Y. Geng, F. Wang, *Macromolecules* **2018**, *51*, 8752.
- [97] Z. Fei, Y. Han, E. Gann, T. Hodsdon, A. S. R. Chesman, C. R. McNeill, T. D. Anthopoulos, M. Heeney, *J. Am. Chem. Soc.* **2017**, *139*, 8552.
- [98] B. Kang, B. Moon, H. H. Choi, E. Song, K. Cho, *Adv. Electron. Mater.* **2016**, *2*, 1500380.
- [99] Z. A. Lamport, H. F. Haneef, S. Anand, M. Waldrip, O. D. Jurchescu, *J. Appl. Phys.* **2018**, *124*, 071101.
- [100] J. N. Haddock, X. Zhang, S. Zheng, Q. Zhang, S. R. Marder, B. Kippelen, *Org. Electron.* **2006**, *7*, 45.
- [101] M. D. Austin, S. Y. Chou, *Appl. Phys. Lett.* **2002**, *81*, 4431.
- [102] A. P. Kam, J. Seekamp, V. Solovyev, C. C. Cedeño, A. Goldschmidt, C. M. S. Torres, *Microelectron. Eng.* **2004**, *73*, 809.
- [103] A. F. Fernández, K. Zojer, *Appl. Phys. Lett.* **2017**, *111*, 173302.
- [104] K. Takagoshi, F. Fujimori, T. Minari, T. Miyadera, T. Hamano, Y. Aoyagi, *Appl. Phys. Lett.* **2007**, *91*, 113508.
- [105] J. Z. Wang, Z. H. Zheng, H. Sirringhaus, *Appl. Phys. Lett.* **2006**, *89*, 083513.
- [106] T. Hirose, T. Nagase, T. Kobayashi, R. Ueda, A. Otomo, H. Naito, *Appl. Phys. Lett.* **2010**, *97*, 083301.
- [107] N. Kumari, M. Pandey, S. Nagamatsu, M. Nakamura, S. S. Pandey, *ACS Appl. Mater. Interfaces* **2020**, *12*, 11876.
- [108] H. Sirringhaus, T. Sakanoue, J.-F. Chang, *Phys. Status Solidi B* **2012**, *249*, 1655.
- [109] A. B. Naden, J. Loos, D. A. MacLaren, *J. Mater. Chem. C* **2014**, *2*, 245.
- [110] Z. He, Z. Zhang, S. Bi, J. Chen, D. Li, *Sci. Rep.* **2020**, *10*, 4344.
- [111] K. Kim, K. Nam, X. Li, D. Y. Lee, S. H. Kim, *ACS Appl. Mater. Interfaces* **2019**, *11*, 42403.
- [112] A. D. Carlo, F. Piacenza, A. Bolognesi, B. Stadlober, H. Maresch, *Appl. Phys. Lett.* **2005**, *86*, 263501.
- [113] S. Illig, A. S. Eggeman, A. Troisi, L. Jiang, C. Warwick, M. Nikolka, G. Schweicher, S. G. Yeates, Y. H. Geerts, J. E. Anthony, H. Sirringhaus, *Nat. Commun.* **2016**, *7*, 10736.
- [114] H. Dong, C. Wang, W. Hu, *Chem. Commun.* **2010**, 46, 5211.
- [115] K. J. Fallon, A. Santala, N. Wijeyasinghe, E. F. Manley, N. Goodeal, A. Leventis, D. M. E. Freeman, M. Al-Hashimi, L. X. Chen, T. J. Marks, T. D. Anthopoulos, H. Bronstein, *Adv. Funct. Mater.* **2017**, *27*, 1704069.
- [116] B. C. Schroeder, T. Kurosawa, T. Fu, Y.-C. Chiu, J. Mun, G.-J. N. Wang, X. Gu, L. Shaw, J. W. E. Kneller, T. Kreouzis, M. F. Toney, Z. Bao, *Adv. Funct. Mater.* **2017**, *27*, 1701973.
- [117] D.-M. Smilgies, *J. Appl. Crystallogr.* **2009**, *42*, 1030.
- [118] S. B. Lee, B. Kang, D. Kim, C. Park, S. Kim, M. Lee, W. B. Lee, K. Cho, *ACS Appl. Mater. Interfaces* **2019**, *11*, 47153.